Zlotnik, S., Fernández, M., Díez, P. and Vergés, J., Modelling Gravitational Instabilities: Slab Break-off and Rayleigh-Taylor Diapirism, *Pure and Applied Geophysics*, Vol. 165, Issue 8, pp. 1491-1510, 2008

# Modelling gravitational instabilities: slab break–off and Rayleigh–Taylor diapirism

## Modelling gravitational instabilities

**Sergio Zlotnik · Manel Fernández · Pedro Díez · Jaume Vergés**

Sergio Zlotnik, Manel Fernández, Jaume Vergés

Group of Dynamics of the Lithosphere (GDL), Institute of Earth Sciences "Jaume Almera", CSIC CSIC Lluís Solé i Sabarís s/n, 08028 Barcelona, Spain Tel.: +34-93-4095410

Fax: +34-93-4110012

E-mail: {szlotnik,mfernandez,jverges}@ija.csic.es

Pedro Díez

Laboratori de Càlcul Numèric, Departament de Matemàtica Aplicada III, Universitat Politècnica de Catalunya Campus Nord UPC, 08034 Barcelona, Spain E-mail: pedro.diez@upc.edu

**Abstract** A new code to solve multiphase viscous thermo–mechanical problems applied to geophysics is presented. Two numerical methodologies employed in the code are described: a level set technique to track the position of the materials and an enrichment of the solution to allow the strain rate to be discontinuous across the interface. These techniques have low computational cost and can be used in standard desktop PCs. Examples of phase tracking with level set are presented in two and three dimensions to study slab detachment in subduction processes and Raileigh–Tailor instabilities, respectively.

The modelling of slab detachment processes includes realistic rheology with viscosity depending on temperature, pressure and strain rate; shear and adiabatic heating mechanisms; density including mineral phase changes and varying thermal conductivity. Detachment models show a first prolonged period of thermal diffusion until a fast necking of the subducting slab results in the break–off. The influence of several numerical and physical parameters on the detachment process is analyzed: the shear heating exerts a major influence accelerating the detachment process, reducing the onset time to one half and lubricating the sinking of the detached slab. The adiabatic heating term act as a thermal stabilizer. If the mantle temperature follows an adiabatic gradient neglecting this heating term must be included, otherwise all temperature contrast are overestimated. As expected, the phase change at 410 km depth due to the olivine–spinel transition facilitates the detachment process due to the increase in negative buoyancy.

Finally, simple plume simulations are used to show how the presented numerical methodologies can be extended to three dimensions.



**Keywords** tectonic plates; subduction; numerical modelling; eXtended Finite Element Method (X–FEM)

## 1 Introduction

Currently available computer codes for geodynamic simulation involve the resolution of a mechanical problem, usually a non–linear flow equation (conservation of mass and momentum), coupled with a thermal problem (conservation of energy). Additional equations are incorporated to describe material parameters. For example the density is computed as a function of pressure and temperature. Strong non–linearities are produced by the constitutive equation which usually is a combination of several power–laws where the viscosity depends on a power of the strain rate.

A main characteristic of this kind of models is the presence of several material phases corresponding to different types of rocks. From the numerical point of view each of these materials is described by a set of parameters defining its mechanical and thermal behaviour. Tracking the location of the material along time is necessary to describe the evolution of the system, including the location of each material phase, though this is not a trivial task since flow problems are naturally described in an Eulerian framework. Several numerical techniques are used in present codes to solve the basic mechanical and thermal equations: finite elements (e.g. Scott et al., 1990; Moresi and Gurnis, 1996), finite differences (e.g. Babeyko et al., 2002; Gerya and Yuen, 2003) and variations of these are the more popular. Nevertheless, to the knowledge of the authors, all present codes in the context of geophysical modelling, use Lagrangian markers to track the location of the materials.



The markers technique consists in using a number, usually large, of Lagrangian points carrying the material parameters. The properties of a point of the Eulerian framework are computed as an average of the markers close to this point. This technique was originally designed to work in a finite differences framework, where the discretization is regular and structured and thus is trivial to identify the markers close to each node. When the mesh becomes non–structured, as with finite elements, the detection of the markers in the proximity of a node is a computationally time consuming task. To reduce the computational time most present multiphase codes run on parallel multiprocessor computers. Despite of the parallelization, the number of operations required is still high and therefore, a technique requiring less computational effort is desirable.

Van Keken et al. (van Keken et al., 1997) study the material tracking problem and compare different tracking techniques to solve an Eulerian multiphase problem. They test three methods: the Lagrangian markers method (named as “tracers” in their work), a marker chain method where the interface between

two materials is discretized using a series of markers and, finally, a field method where the material properties are described by a continuous field similar to temperature. They conclude that the Lagrangian marker approach is the most accurate method, alerting about the large number of markers needed. This huge number poses severe restrictions to the application of the technique to three dimensional problems. According to van Keken et al. (van Keken et al., 1997) two dimensional isoviscous materials require, at least 10 to 100 markers per element. For more realistic rheologies this ratio even increases.

Present applications of the marker technique use much more than 10 markers per element. The simulations of lithospheric structures related to subduction zones done by Gerya and Gorczyk (Gorczyk et al., 2006) use, in average, $1.25 \times 10^5$ markers per element. That is, an amazing grand total of 10 billion markers. With these extremely high resolutions they can track meter–size structures. Leaving aside the super–populated simulations, in most 2D models the estimation of 100 markers per element is fair.

When models move from 2D to 3D, the relationships between markers and elements become a serious restriction. To maintain the resolution used by Gerya and Gorczyk (Gorczyk et al., 2006) in a three dimensional model, $1 \times 10^{15}$ markers are needed. This posses severe computational restrictions: if each marker employs only twelve bytes of memory —a minimum lower bound to store only its position— the amount of required memory is 366 times greater than the memory of the present world biggest computer, which has 32768 giga bytes of memory.



In this work a different approach to track the material phases is proposed. The idea is to reduce computational effort obtaining similar results to those obtained using markers. This reduction is achieved mainly by the description of the location of materials with a number of nodes similar to those used in the mechanical problem. In other words, the same interpolation (the same mesh) is used for the materials location and for the velocity field. Therefore, when moving from 2D to 3D, the tracking of materials does not add extra points to those describing the 3D velocity field. The similar number of nodes used to interpolate velocity and material locations results in a similar accuracy for both fields.

Moreover, the level set technique does not require averaging the material properties from markers to nodes, nor the temperature and pressure from nodes to markers. The level set approach may describe changes in the shape (topology) of the phases, thus allowing for the representation of detaching drops, merging bubbles, etc. This feature of the level set method is of great interest when used, for instance, to

model slab break–off phenomena. The topological change in the interface due to the separation of the slab can be naturally handled by the level set function.

In addition to the level set method, the solution is improved in the vicinity of the interface using an *enrichment* technique. A standard linear finite element (or finite difference) solution allows for changes in its derivative only over the edges of the elements; whereas within the elements the solution is linear. The enriched solution allows for describing discontinuities in the gradient of the solution across the interface described by the level set, whether or not this interface conforms with the element edges.

The enrichment technique is particularly suitable for multiphase problems in which the strain rate is discontinuous across the interface due to the continuity of stress and the jump in the viscosity across the interface. None of the methods tested in (van Keken et al., 1997) is well suited to resolve this discontinuity. Instead, it is approximated by a continuous function and effectively smeared out over a few grid elements (van Keken et al., 1997). The enrichment technique adds dynamically some degrees of freedom to the mechanical solution to catch the discontinuity exactly where it is expected to happen, i.e. over the interface described by the level set.



These two techniques, *level sets* and *enrichment* are designed to work together and to fit naturally in a finite element framework. This combination is usually called eXtended Finite Element Method (X–FEM) and is commonly used in engineering problems to track materials (e.g. Chessa and Belytschko, 2003; Moës et al., 2003), to model crack growth (e.g. Belytschko and Black, 1999; Stolarska et al., 2001), to model holes and inclusions (Sukumar et al., 2001), etc.

The aim of this paper is to introduce the X–FEM methodology to study geodynamic processes and to show its numerical capabilities. To this goal we use two complex geophysical examples: i) a 2D simulation of the break–off and sinking of a subducting lithospheric slab considering thermo–mechanical coupling and non–linear rheology; and ii) a 3D simulation of a Rayleigh–Taylor instability using a simple phase-wise constant viscosity in a cubic space domain. We compare the obtained results with those from previous studies using the marker technique and we show some desirable properties of X–FEM: its reduced computational cost, its straightforwardness in moving from 2D to 3D and the ability of the level sets to reproduce changes in topology, as it is the case of drops.

## 2 Extended Finite Elements

### 2.1 Level sets and phase tracking

The location of the interface between two materials is described by a level set function $\phi$ on the computational domain. The interface is defined by the curve (the surface in 3D) where the level set vanishes. Thus, the sign of $\phi$ describes the material domains using the following convention

$$\phi(\mathbf{x},t) = \begin{cases} > 0 \text{ for } \mathbf{x} \text{ in material domain 1} \\ = 0 \text{ for } \mathbf{x} \text{ on the interface} \\ < 0 \text{ for } \mathbf{x} \text{ in material domain 2} \end{cases} \tag{1}$$

where $\mathbf{x}$ stands for a point in the simulation domain and $t$ is the time. Initially, $\phi$ is taken as a signed distance to the interface. Far enough from this interface, $\phi$ is truncated by maximum and minimum cutoff values.

Since this approach does not require that the interface conforms to the edges of the elements, the same mesh can be used throughout the entire simulation and remeshing procedures are not required. In practice, the function $\phi$ is discretized with the finite element mesh (same as velocities or temperatures) and therefore the location of the interface is described with the same accuracy of the mechanical and thermal problem. While the model evolves and the materials move, the level set is updated with the velocity field $\mathbf{u}$ obtained from the mechanical problem by solving a pure–advective equation



$$\dot{\phi} + \mathbf{u} \cdot \nabla\phi + \phi \cdot \nabla\mathbf{u} = 0. \tag{2}$$

The last term of the right hand side of (2), $\phi \cdot \nabla\mathbf{u}$, is neglected due to the incompressibility hypothesis (see section 3.1, equation (7)).

The numerical integration of this equation can be performed using several algorithms, for example, Runge–Kutta methods or Taylor–Galerkin methods. Details on the implementation of the space and time discretization of the level set can be found in (Zlotnik et al., 2007).

The level set function, $\phi$, is usually chosen to be a distance function, although it is well-known that the solution to the evolution equation (2) (with a distance function as initial condition) does not necessarily remain a distance function and, sometimes, a procedure is required to reinitialize it without changing its zero level set. Different techniques have been proposed in many papers to preserve the level set to the signed distance function (e.g. Chopp, 1993; Sussman et al., 1994; Gómez et al., 2005). However, as demonstrated

in the examples given in section 4 and 5 and in the tests performed in (Zlotnik et al., 2007), for the current application this method is sufficiently accurate and it does not require any post-process to reconstruct the distance shape.

### 2.2 The mechanical problem and the enriched solution

The enrichment technique is introduced in this section applied to the mechanical flow problem governed by the Stokes equation (see formulation in the next section). This equation is discretized in space using a mixed formulation, where the velocity and pressure fields are interpolated differently. Here the well-known mini-element is used (Donea and Huerta, 2002). This triangular element is composed by three pressure nodes at the vertices (linearly interpolated) and four velocity nodes (three linear nodes at the vertices and one central quadratic node). Denoting by $\mathcal{N}$ the set of indices associated with the velocity nodes, the approximation of the velocity $\mathbf{u}_h$ reads

$$\mathbf{u}(\mathbf{x},t) \simeq \mathbf{u}_h(\mathbf{x},t) = \sum_{j\in\mathcal{N}} N_j(\mathbf{x})\,\mathbf{u}_j(t) \tag{3}$$

where $\mathbf{u}_j$ is the velocity vector in the node $j$. This is the usual finite element interpolation in terms of the shape functions $N$. In order to improve the ability of the interpolation to represent gradient discontinuities across the interface, the enrichment technique add some extra degrees of freedom to the interpolation of the velocity (Moës and Belytschko, 2002, Zlotnik et al., 2007)

$$\mathbf{u}_h(\mathbf{x},t) = \sum_{j\in\mathcal{N}} \mathbf{u}_j(t)\,N_j(\mathbf{x}) + \sum_{j\in\mathcal{N}_{enr}} \mathbf{a}_j(t)\,M_j(\mathbf{x}) \tag{4}$$

where $\mathcal{N}_{enr}$ denotes the set of enriched nodes. The interpolation functions $M_j$ associated with the enriched degrees of freedom $\mathbf{a}_j$ are built using the standard finite elements shape function $N_j$ and a ridge function $R$ defined as

$$R(\mathbf{x}) = \sum_{j\in\mathcal{N}_{enr}} |\phi_j|\,N_j(\mathbf{x}) - \left|\sum_{j\in\mathcal{N}_{enr}} \phi_j\,N_j(\mathbf{x})\right|. \tag{5}$$

The ridge is defined such that is only different from zero in the elements containing part of the interface. This technique improves the solution near the interface described by the level set. Figure 1 shows how the enrichment technique modifies the solution inside the elements crossed by the interface between materials. In these elements the enrichment allows the solution to catch the kink produced by the jump of the material properties. Pressure is enriched in the same way as for velocity. Note that in the definition of the ridge

the shape functions are not required to be linear. For a detailed description of the implementation of the enrichment technique we refer the reader to (Zlotnik et al., 2007).

## 3 Physical model

In order to show the abilities of the X–FEM, we apply it to a multiphase creep-flow problem. Moreover, a realistic geodynamical model including non-linear rheology allows us to compare results with previuos works.

The fundamental physical equations governing the dynamics of the model, namely, conservation equations of mass, momentum, and energy are presented. These equations are standard in geodynamic models (e.g. Schott and Schmeling, 1998; Gerya and Yuen, 2003; Manea et al., 2006; van Hunen et al., 2004) and can be employed to model any multiphase viscous fluid coupled with heat transport. Applications include, salt tectonics and diapir formation models (e.g. Poliakov et al., 1993; S. Zaleski, 1992) or entrainment of a dense D" layer by mantle convection. The equations are presented in their compact or matrix form, in which the bold symbols denote vector variables.



### 3.1 Basic equations

The mechanical problem requiring conservation of momentum is governed by the Stokes equation in which, as usual for creeping flows, the inertia term is neglected. The equation, considered in its quasi–static version, can by written in terms of velocity $\mathbf{u}$ and pressure $p$ as

$$\nabla \cdot (\eta \nabla^{\mathrm{s}} \mathbf{u}) + \nabla p = \rho\, \mathbf{g} \tag{6}$$

where $\eta$ is the viscosity, $\rho$ the density, and $\mathbf{g}$ the gravitational acceleration vector. The operator $\nabla^{\mathrm{s}}$ is defined as $1/2(\nabla^{\mathrm{T}} + \nabla)$. Solving the Stokes problem (6) provides velocities and pressures at every time. As the constitutive equation described in section 3.2, depends on the velocity gradient, a non–linear behaviour is introduced. The transient equation (6) is said to be pseudo–static as a consequence of neglecting inertia terms (infinite Prandtl number approximation), because it does not contain any explicit time dependence. The transient character of the solution is due to the motion of the phases and to the temperature field evolution.

As in the majority of existing codes (e.g. van Keken et al., 1997; Gerya and Yuen, 2003; King et al., 1990), and despite its lack of consistency for the mass conservation equation, we have assumed incompressibility and the Boussinesq approximation, that is, the density is taken as constant in all terms except for the buoyancy force in the right hand side of equation (6). Then, the mass conservation equation reads

$$\nabla \cdot \mathbf{u} = 0 \tag{7}$$

Although compressibility is not incorporated in the continuity equation, it is considered in terms of thermal expansion and phase changes which modify material densities and also in terms of adiabatic heating, which is incorporated in the energy conservation equation.

Usually, viscosity $\eta$ and density $\rho$ are temperature dependent and consequently the mechanical and thermal problem are coupled.

The conservation of energy equation reads

$$\rho\, C_p\big(\dot{T} + \mathbf{u}\nabla T\big) = \nabla \cdot (k \nabla T) + \rho f \tag{8}$$

where $T$ is temperature, $C_p$ the isobaric heat capacity, $k$ the thermal conductivity, and $f$ a heat source term. Solving the thermal problem provides nodal temperatures, which are used to calculate the density $\rho$, the thermal conductivity $k$ and the viscosity $\eta$. For mantle simulations the heat source term $f$ is composed by three sources: a constant term, $f_r$ corresponding to the decay of radioactive elements; an adiabatic heating term for accounting for the heat exchange due to compression and decompression of materials being approximated as $f_{ah} \approx T\alpha\rho u_z g_z$ (Gerya et al., 2004) where $\alpha$ denotes the thermal expansion and subscript $z$ refers to the vertical component of the vectors; and finally a shear heating term, $f_{sh}$, associated with the mechanical heat dissipation. The shear heating is computed from the solution of the mechanical problem (6) as $f_{sh} = \sigma_{ij}\dot{\varepsilon}_{ij}$, where $\sigma$ is the deviatoric stress tensor and $\dot{\varepsilon}$ the deviatoric strain rate tensor. This dependence of the heat source on the strain rate and stress enhance the coupling between the thermal and mechanical equations.



### 3.2 Constitutive equation

Fluids are characterized by a constitutive equation in which stress is a function of strain rate. In Newtonian fluids this function is linear, whereas in non-Newtonian fluids the strain rate is proportional to the $n$th power of the stress.

Rheological behaviour of the mantle involves both Newtonian (diffusion) and non-Newtonian (dislocation) deformation mechanisms (Karato and Wu, 1993). Each one of these mechanisms can be stated using a power-law, in which the viscosity depends on temperature, pressure and strain rate as follows (Ranalli, 1995)

$$\eta_{\text{creep}} = (\dot{\varepsilon}_{\text{II}})^{\frac{1-n}{n}} (A)^{\frac{-1}{n}} \exp\left(\frac{E + p\Delta V}{nRT}\right), \tag{9}$$

where $\dot{\varepsilon}_{\text{II}} = (\frac{1}{2}\dot{\varepsilon}_{ij}\dot{\varepsilon}_{ij})^{1/2}$ is the second invariant of the deviatoric strain rate tensor, $n$ the exponent of the power-law, and the material parameters are: the activation energy $E$, the activation volume $\Delta V$ and the material constant $A$. This expression is truncated if the resulting viscosity is either greater or lower than two imposed cutoff values ($10^{18}$ to $10^{24}$ Pa s$^{-1}$). To include both deformation mechanisms, two equations of the form of (9) are used. The effective viscosity is computed as the harmonic mean of the two viscosities obtained.



## 4 Slab break–off

The slab break–off problem is specially well suited to demonstrate the ability of the level set to reproduce changes in the topology of the interface, for example the separation of part of the material. Moreover, the obtained results are compared with previous simulations (e.g. Yoshioka and Wortel, 1995; Davies and von Blanckenburg, 1995; Gerya et al., 2004) all using Lagrangian markers. This comparison allows us to check the correctness of our code and to show the capability of the X–FEM technique to obtain similar results as with the marker technique. In addition, we explore the role of shear heating, adiabatic heating, mineral phase changes and plate thickness as factors controlling the slab detachment. Rheological factors, like the maximum imposed viscosity are also studied.

Several subduction zones exhibit a clear gap in the hypocentral distribution between 100 and 300 km depth. These gaps are believed to be an expression of a mechanically decoupling of the descending slab, or slab break–off, relative to the subducting lithospheric plate. This interpretation is supported by seismic tomography (Xu et al., 2000), theoretical considerations (Blanckenburg and Davies, 1995) and numerical modelling (Gerya et al., 2004). Regions where the slab break–off has been proposed to operate are the New Hebrides (Isacks and Molnar, 1969), the Carpathians (Wortel and Spakman, 2000), the Hellenic arc (Spakman, 1988), the Alps (Blanckenburg and Davies, 1995) and Iran (Molinaro et al., 2005).

The main gravitational forces acting on the subducting lithosphere are the negative buoyancy of the slab (slab pull), the ridge push, and the negative and positive buoyancy of the mineral phase changes from olivine to wadleyite at 410 km depth and from spinel to perovskite and magnesiowüstite at 660 km depth. In order to include these forces in our model, the density is calculated as a function of the temperature and pressure as follows (Schubert et al., 2001)

$$\rho = \rho_0[1 - \alpha(T - T_0)][1 + \beta(p - p_0)], \tag{10}$$

where $\alpha$ and $\beta$ are, respectively, the thermal expansion and compressibility coefficients, and $T_0$ and $p_0$ are reference values at surface.

The two mineral phase transitions incorporate sharp increments in the density field. The temperature and pressure region of stable mineralogy is delimited by the Claperyron curves of the mineral transition reactions (see Figure 2). Therefore, the density $\rho_0$ in equation (10) is calculated as a reference olivine mantle density plus a $\Delta\rho$ depending on the temperature–pressure region, as $\rho_0 = \rho_{ol} + \Delta\rho$ where

$$\Delta\rho = \begin{cases} 0 & \text{if } T\text{-}p \text{ is in the olivine region} \\ \Delta\rho_{sp} & \text{if } T\text{-}p \text{ is in the wadsleyite region} \\ \Delta\rho_{per} & \text{if } T\text{-}p \text{ is in the perovskite region.} \end{cases}$$

The parameters used to delimit regions are listed in Table 1.

It is worth noting that the ridge push force is not included in the model because the detachment process is expected to happen after cessation of active subduction. In other words, in our simulation the convergence velocity is zero.

The thermal conductivity of rocks also depends on temperature and pressure. At high temperatures (T $\geq$ 1500 K) the electromagnetic radiation becomes important enough to be included as an extra heat transfer mechanism (Hofmeister, 1999). The following empirical expression, which includes both conductive and radiative effects, is used (Clauser and Huenges, 1995)

$$k = \mathrm{a} + \left(\frac{\mathrm{b}}{T + \mathrm{c}}\right) \exp(\mathrm{d}\, p), \tag{11}$$

where a= 0.73, b= 1293, c= 77, and d= 0.00004. Note that this expression is dimensional ($\mathrm{Wm^{-1}K^{-1}}$) and therefore temperature and pressure must be expressed in K and MPa, respectively.

The initial configuration of our simulations corresponds to a subduction zone with the slab reaching a depth of 400 km, see Figure 3 (b). The initial thermal structure has been generated by a previous simulation

where a horizontal velocity of 2.5 cm $yr^{-1}$ is imposed on the subducting plate while the overriding plate is fixed.

This model involves two material phases described by a level set: the lithosphere and the underlying mantle. In our approach we have used the thermal definition of lithosphere and therefore the interface between the lithosphere and the sublithospheric mantle coincides with the initial 1300°C isotherm. Actually, the level set and the 1300°C isotherm roughly coincides during the whole evolution of the model due to the low thermal conductivity values of rocks which makes advection to be dominant over diffusion. In addition, the density $\rho_0$ assigned to the lithospheric material is an average bulk density for the lithosphere and incorporates the lower density of crustal materials.

Another configuration that might be used —and would give more accurate results— to model slab break-off, is to different materials for the crust and the mantle. We discarded this option because of the reduced thickness of the oceanic crust (usually $< 10$ km) which requires to greatly increase the number of elements and consequently the computation time. Since the main goal of this example is to show the X–FEM capabilities applied to geodynamical simulations, we consider that the chosen material configuration is a good trade off between computation time and accuracy of the model.

The initial temperature structure of the subducting plate is horizontally homogeneous. Its thickness is 100 km and id defined by the 1300°C isotherm, which corresponds to a plate older than 80 Ma. During the evolution of the model the temperatures at the surface and at the bottom of the model (1000 km depth) are imposed to be zero and 1771°C, respectively. Across the side walls of the model domain a null heat flux is imposed.

Assuming that the detachment process will start after the cessation of plate convergence, the surface of the model is considered as a free surface and no velocity is imposed on it. Free slip conditions are used in the bottom and side walls of the domain.

### 4.1 Results

A reference model has been generated using the parameters listed in Table 1. The calculated initial viscosity is shown in Figure 3 (c) and profiles of mechanical and thermal properties are shown in Figure 4. The evolution of the detachment process corresponding to the reference model can be followed in Figure 5. After a period of approximately 24 Myr of thermal diffusion, the slab undergoes a necking process lasting

$\sim$ 2 Myr and localized at a depth of 150–200 km. Necking concentrates extensive deformation in a narrow zone of the slab producing large stresses and shear heating (Figure 5, 25 Myr row). The slab detachment is characterized by a high strain rate and a spread shear heating all around the slab (Figure 5, 26 Myr row). The shear heating controls the dynamics of the system not only during the necking, but also during the sinking of the detached slab. Values of shear heating up to $3 \times 10^{-5}$ W m$^{-3}$ are obtained. This amount of heating is about three orders of magnitude larger than the radioactive heating of the mantle. Similar values were reported by (Gerya et al., 2004). When shear heating is not considered the detachment occurs about 20 Myr later and the sinking velocity of the slab is about one third of the velocity obtained with the reference model.

The adiabatic heating term is important to reproduce the behaviour of the mantle at great depths. Numerically it acts reducing the coupling between the mechanical and the thermal equations. As shown in Figure 6, the obtained mantle structure for a model with the same initial temperature distribution but lacking the adiabatic heating term in the energy conservation equation greatly differs from the reference solution, even before the detachment occurs. Therefore, excluding the adiabatic heating produces that hot material from the deeper part of the model is upwelled forming large convective cells that involve the whole mantle. The mantle surrounding the slab at 200–300 km depth is hotter than in the reference model enhancing the thermal diffusion and accelerating the detachment process, which happens about 1 Myr before. It must be noted however that the initial temperature distribution within the sublitospheric mantle "incorporates an adiabatic gradient which is somehow inconsistent with neglecting the adiabatic heating term in the energy equation. Therefore Figure 6 (a) reflects an extremely unstable mantle as a consequence of an initial geotherm which is too hot for a fully incompressible mantle.

The role of mineral phase changes at 410 and 660 km depth is crucial in determining the depth distribution of the mantle density. It is well known that the endothermic character of the olivine-wadleyite reaction developing at 410 km depth increases the slab pull force, and therefore helps the detachment to occur. According to this, the slab detachment may be delayed by about 20 Myr with respect to the reference model when the olivine–wadsleyite phase transition is not considered. Moreover, the maximum reached stress is about one half of that obtained with the reference model. The role of the spinel–to–perovskite/magnesiowüstite exothermic transition occurring at 660 km depth is less noticeable. Due to its exothermic character this transition prevents the penetration of the cold slab through the discontinuity.

In the absence of this phase change, the detachment occurs at the same time and the maximum stresses and strain rates are similar to those obtained with the reference model and happen at similar times and depths. The main obvious difference is that the sinking velocity of the detached slab is not reduced when reaches 660 km depth since, in this case, any discontinuity is imposed at this depth.

The effects of varying the mantle rheology have been also examined. Increasing the upper bound of the allowed viscosity to values of $10^{26}$ delays the break–off by about 15 Myr although it is not enough to inhibit the detachment of the slab. The time at which the maximum strain rate is reached suffers also a similar delay but the maximum stress occurs 2 Myr later when compared with the reference model. In fact, the time at which the strain rate reaches its maximum value is a good proxy of the detachment time, while the time interval during which the stress is maximum is a proxy of the necking process.

Finally, reducing the lithospheric thickness to 70 km (the reference lithosphere is 100 km thick) produces that the slab detaches 2 Myr earlier. The break–off occurs at a depth about 60 km shallower and the magnitudes of the generated stresses are almost a half with respect to the reference model. Relevant results like the maximum values of strain rate second invariant, shear heating, stress second invariant and velocity are listed in Table 2 together with the corresponding time and average depth at which they have been calculated.

## 5 Rayleigh–Taylor instabilities

Compositional differences within the crust and mantle can produce local density perturbations in which relatively light material is embedded in a denser ground. In these situations, the lighter body exerts a positive buoyancy that can result in the development of diapirism. Examples of that are salt domes, granitic batholiths, or the entrainment of a chemically distinct D" layer in the lower mantle. Although most of these processes are also temperature dependent, in this section we will only consider, for the sake of simplicity, the compositional aspect (multiphase mechanical behaviour) in order to show the capabilities of the level set in 3D simulations.

Then, our simulation is based on an isothermal Rayleigh–Taylor instability that develops in a cubic domain, which has been discretized with a mesh of 23461 tetrahedra (element size is approximately 1/15 of the cubic domain side). The equations of conservation of momentum (6) and mass (7) are solved imposing: i) free slip conditions along the walls of the cube; ii) an initial sinusoidal perturbation on the phase boundary

—level set— of amplitude $A = 0.05$ (dimensionless) and wavelength = 1; iii) a density ratio between the upper and lower material of $\rho_1/\rho_2 = 1.003$.

Figure 7 shows the evolution of a Rayleigh-Taylor instability with a viscosity ratio $\eta_1/\eta_2 = 1$ and a dimensionless lower layer thickness of 1/3 . The plotted surface corresponds to the interface between the two materials described by the level set. The evolution of the diapir follows the three stages described by Whitehead and Luther (Whitehead Jr and Luther, 1975) for a thin layer of a low Reynolds number fluid: the first stage of evolution, Figure 7 (a), is described by a linear Rayleigh–Taylor instability. In the second stage, Figure 7 (b), the fluid moves upward as a circular column surrounded by relatively broad regions of descending material. In the third stage, Figure 7 (c) and (d), fully mature structures are formed, in this case the level set looses its radial symmetry and significant folds are developed at the base and the tail of the level set. These asymmetry and folds are related to the cubic shape and proximity of the walls of the model domain. When the level set reaches the upper boundary of the model domain the buoyant lower material is in contact with the top of the domain. This contact is not an interface between different materials and thus is not drawn. In fact, the level set function does not vanishes at these points. Therefore, the moving inteface between materials adopts a wineglass shape as shown in Figure 7 (c) and (d).

Figure 8 shows some snapshots of models with different viscosity ratios and different initial thicknesses of the buoyant underlying material that are used as simulation benchmark. Snapshots correspond to similar times after the modelling initiation for the four cases. In general terms, the viscosity ratio controls the size of the diapir head and the velocity at which the initial stratification overturns (Figure 8 (a) and (b)). On the other hand, the initial thickness of the underlying layer mainly controls the velocity at which the head of the diapir rises and hence, the length of the tail.

All these examples show the capability of level sets to reproduce the geometry of the interface evolution between two (or more) deforming materials in three dimensions.

## 6 Discussion and Conclusions

The analysis presented in this study allow us for drawing the following conclusions:

- Level sets, as used here, allows for describing the interface between two deforming materials with the same resolution as for the mechanical problem. Therefore, the minimum size of a body delimited by the level set is given by the element size. This is a very different characteristic from the marker technique,

which can increment the number of markers independently of the element size. However, markers also require a dense grid to increase the resolution of the problem penalizing the computer time. Moreover, the X–FEM approach described here is especially well suited to use adaptive mesh refinement. This allows increasing locally accuracy of the numerical method and obtaining an accurate answer with the minimum computational cost.

- The transport of the interface described by the level set may introduce some numerical oscillations. Several ad hoc techniques have been proposed to avoid this undesirable behaviour. Nevertheless, our experience shows that for simple geometries, like the presented 2D and 3D numerical experiments, fair results are obtained even if the distance shape of the level set in not preserved.
- Using level set and enriched solution techniques (X–FEM) implies a very cheap computational cost. Running the thermo–mechanical 2D code for the presented subduction simulations (including non–linear rheology, phase changes, adiabatic heating, shear heating, etc.) lasts less than 12 hours in a desktop PC with a single 3 GHz processor and 2 GB of memory.
- A very attractive advantage of level sets its straightforwardness in moving to 3D simulations: the simplicity of the coding is similar to the 2D case. Moreover, the increase in the computational cost for the 3D case is much lower than for the markers approach. The presented 3D simulations of Rayleigh–Taylor instabilities lasted 50 hours each with the same computer as used for 2D modelling.
- The results obtained from the subducting slab detachment experiments are quantitatively similar to those found in previous studies demonstrating the correct behaviour of the code. The enrichment technique allows for accurately reproduce the strain rate discontinuities produced across the interface due to sharp viscosity contrasts between the two modelled fluids.
- The numerical experiments shown in the present study use only one level set to describe a two phase fluid problem. Nevertheless, we have done some tests for a multiphase fluid problem using a larger number of level sets and obtaining successful results.

## Acknowledgments

This research has been supported by Ministerio de Educación y Ciencia, Grants DPI2007-62395, SAGAS CTM2005-08071-C03-03/MAR and the Spanish Team Consolider-Ingenio 2010 nrCSD2006-00041. We thank Vlad Manea and an anonymous reviewer for discussion and comments.

**References**

A. Y. Babeyko, S. V. Sobolev, R. B. Trumbull, O. Oncken, and L. L. Lavier. Numerical models of crustal scale convection and partial melting beneath the Altiplano–Puna plateau. *Earth Planet. Sci. Lett.*, 199: 373–388, 2002.

T. Belytschko and T. Black. Elastic crack growth in finite elements with minimal remeshing. *International Journal for Numerical Methods in Engineering*, 45(5):601–620, 1999.

F. Von Blanckenburg and J. H. Davies. Slab breakoff: a model for syncollisional magmatism and tectonics in the Alps. *Tectonics*, 14:120–131, 1995.

J. Chessa and T. Belytschko. An extended finite element method for two–phase fluids. *Transactions of the ASME*, pages 10–17, 2003.

D. L. Chopp. Computing minimal surfaces via level set curvature flow. *Journal of Computational Physics*, 106:77–91, 1993.

C. Clauser and E. Huenges. Thermal conductivity of rocks and minerals. In T. Ahren, editor, *Rock Physics and Phase Relations*, AGU Reference Shelf, part 3, pages 105–126. AGU, Washington DC, third edition, 1995.

J. H. Davies and F. von Blanckenburg. Slab breakoff: a model of lithosphere detachment and its test in the magmatism and deformation of collisional orogens. *Earth Planet. Sci. Lett.*, 129:85–102, 1995.

J. Donea and A. Huerta. *Finite Element Methods for Flow Problems*. Wiley, Chichester, West Sussex PO19 8SQ, England, 2002.

T. V. Gerya and D. A. Yuen. Characteristics–based marker–in–cell method with conservative finite–differences schemes for modeling geological flows with strongly variable transport properties. *Phys. Earth Planet. Inter.*, 140(4):293–318, 2003.

T. V. Gerya, D. A. Yuen, and W. V. Maresch. Thermomechanical modelling of slab detachment. *Earth Planet. Sci. Lett.*, 226:101–116, 2004.

P. Gómez, J. Hernández, and J. López. On the reinitialization procedure in a narrow-band locally refined level set method for interfacial flows. *Int. J. Numer. Meth. Engng*, 63:1478–1512, 2005.

W. Gorczyk, T. V. Gerya, J. A. D. Connolly, D. A. Yuen, and M. Rudolph. Large–scale rigid–body rotation in the mantle wedge and its implications for seismic tomography. *Geochem. Geophys. Geosyst.*, 7(5), 2006. doi:10.1029/2005GC001075.

A. M. Hofmeister. Mantle values of thermal conductivity and the geotherm from phonon lifetimes. *Science*, 283:1969–1706, 1999.

B. Isacks and P. Molnar. Mantle earthquake mechanisms and the sinking of the lithosphere. *Nature*, 223: 1121–1124, 1969.

S.-I. Karato and P. Wu. Rheology of the upper mantle: a synthesis. *Rev. Science*, 260:771–778, 1993.

S. D. King, A. Raefsky, and B. H. Hager. ConMan: vectorizing a finite element code for incompressible two–dimensional convection in the Earth's mantle. *Phys. Earth Planet. Inter.*, 59:195–207, 1990.

V. C. Manea, M. Manea, V. Kostoglodov, and G. Sewell. Intraslab seismicity and thermal stress in the subducted Cocos plate beneath central Mexico. *Tectonophysics*, 420(3–4):389–408, 2006.

N. Moës, M. Cloirec, P. Cartaud, and J. F. Remacle. A computational approach to handle complex microstructure geometries. *Computer Methods in Applied Mechanics and Engineering*, 192:3163–3177, 2003.

M. Molinaro, H. Zeyen, and X. Laurencin. Lithospheric structure beneath the south–eastern Zagros mountains, Iran: recent slab break–off? *Terra Nova*, 17:1–6, 2005.

L. N. Moresi and M. Gurnis. Constraints on lateral strength of slabs from 3–D dynamic flow models. *Earth Planet. Sci. Lett.*, 138:15–28, 1996.

A. N. B. Poliakov, R. van Balen, Yu. Podladchikov, B. Daudre, S. Cloetingh, and C. Talbot. Numerical analysis of how sedimentation and redistribution of surficial sediments affects salt diapirism. *Tectonophysics*, 226:199–216, 1993.

G. Ranalli. *Rheology of the Earth*. Chapman and Hall, 2–6 Boundary Row, London, second edition, 1995.

P. Julien S. Zaleski. Numerical simulation of Rayleigh–Taylor instability for single and multiple salt diapirs. *Tectonophysics*, 260:55–69, 1992.

B. Schott and H. Schmeling. Delamination and detachment of a lithospheric root. *Tectonophysics*, 296: 225–247, 1998.

G. Schubert, D. L. Turcotte, and P. Olson. *Mantle Convection in Earth and Planets*. Cambridge University Press, UK, 2001.

D. K. Scott, A. Raefsky, and B. H. Hager. ConMan: a vectorizing a finite element code for incompressible two–dimensional convection in the Earth's mantle. *Phys. Earth Planet. Inter.*, 59:195–2007, 1990.

W. Spakman. *Upper mantle delay time tomography with an application to the collision zone of Eurasian, African and Arabian plates.* PhD thesis, Univ. of Utrech, Utrech, The Netherlands, 1988.

M. Stolarska, D. L. Chopp, N. Moës, and T. Belytschko. Modelling crack growth by level set in the extended finite element method. *International Journal for Numerical Methods in Engineering*, 51:943–960, 2001.

N. Sukumar, D. L. Chopp, N. Moës, and T. Belytschko. Modeling Holes and Inclusions by Level Sets in the Extended FiniteElement Method. *Computer Methods in Applied Mechanics and Engineering*, 190: 6183–6200, 2001.

M. Sussman, P. Smereka, and S. Osher. A level set approach for computing solutions to incompressible two-phase flow. *Journal of Computational Physics*, 114:146–159., 1994.

J. van Hunen, A. P. van Den Berg, and N. J. Vlarr. Various mechanisms to induce present–day shallow flat subduction and implications for the younger Earth: a numerical parameter study. *Phys. Earth Planet. Inter.*, 146:179–194, 2004.

P. E. van Keken, S. D. King, H. Schmeling, U. R. Christensen, D. Numeister, and M.-P. Doin. A comparison of methods for the modeling of thermochemical convection. *J. Geophys. Res.*, 102(B10):22477–22495, 1997.

J. A. Whitehead Jr and D. S. Luther. Dynamics of laboratory diapir and plume models. *J. Geophys. Res.*, 80:705–717, 1975.

M. J. R. Wortel and W. Spakman. Subduction and slab detachment in the Mediterranean–Carpathian region. *Science*, 290:1910–1917, 2000.

P. F. Xu, R. M. Sun, F. T. Liu, Q. Wang, and B. Cong. Seismic tomography showing, subduction and slab breakoff of the Yangtze block beneath the Dabie—Sulu orogenic belt. *Chin. Sci. Bull*, 45:70–74, 2000.

S. Yoshioka and M. J. R. Wortel. Three–dimensional numerical modeling of detachment of subducted lithosphere. *J. Geophys. Res.*, 100(B10):20223–20244, October 1995.

S. Zlotnik, P. Díez, M. Fernández, and J. Vergés. Numerical modelling of tectonic plates subduction using X–FEM. *Computer Methods in Applied Mechanics and Engineering*, 196:4283–4293, 2007.

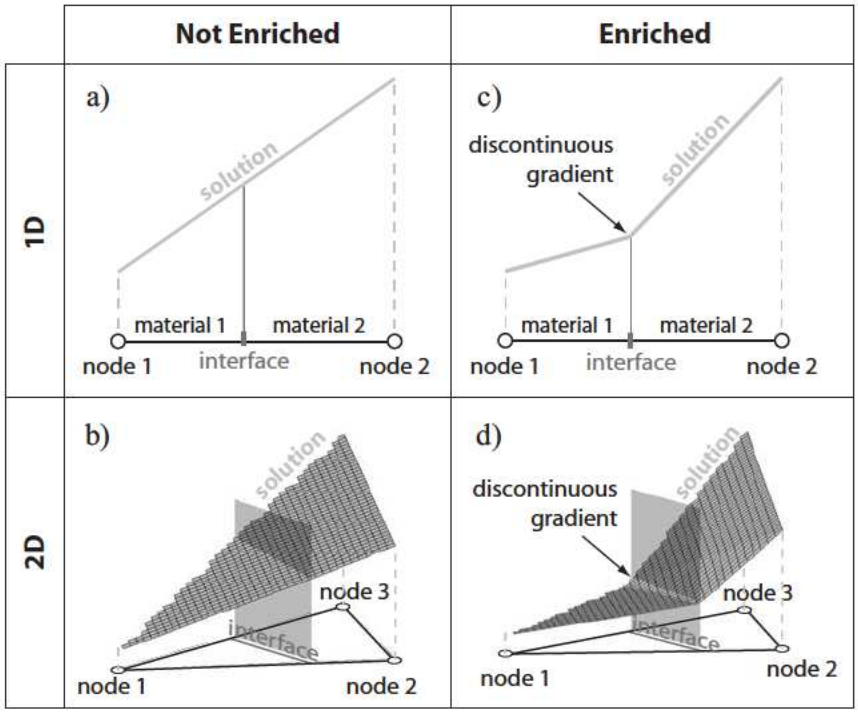


**Fig. 1** The ability of the enriched solution to have a discontinuous gradient is illustrated. The velocity gradient (and strain rate) will be discontinuous across the interface caused by the continuity of stress and the change of viscosity.

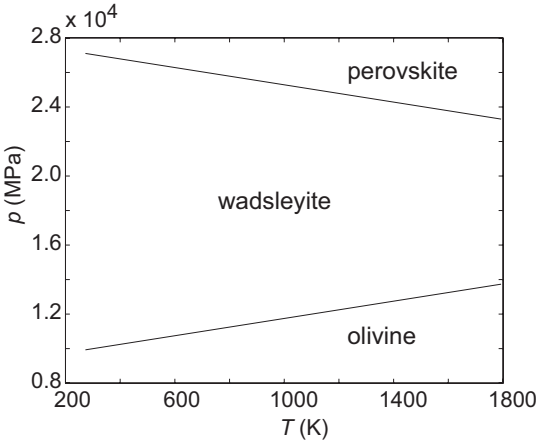


**Fig. 2** Phase diagram indicating stable mineral phases in the temperature–pressure plane. The phase diagram is divided into three regions corresponding to three distinct minerals: olivine, wadsleyite and perovskite.

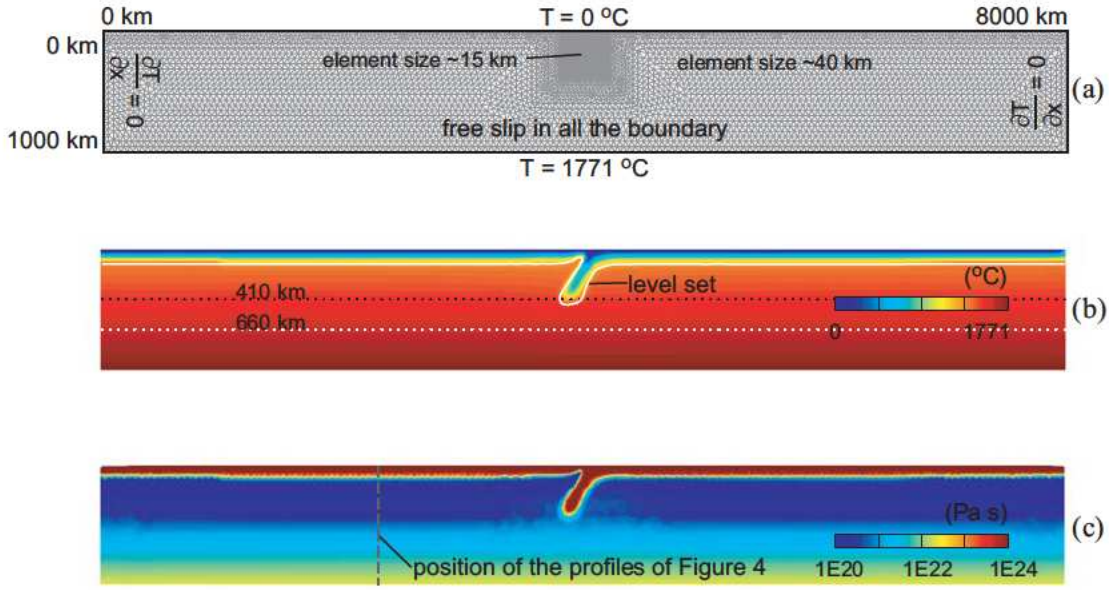


**Fig. 3** (a) Mesh and boundary conditions used to simulate slab detachment, (b) initial temperature distribution, the white line represents the level set location, dotted lines represent phase transitions. (c) viscosity field calculated with initial temperature, pressure and strain rate.

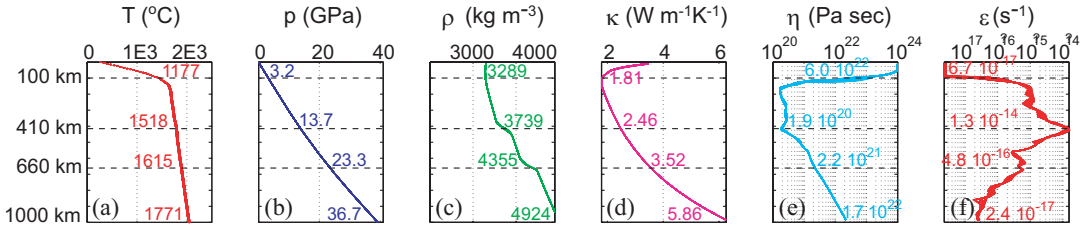


**Fig. 4** Profiles of mantle properties at the beginning of the simulation. Values at 100, 410, 660 and 1000 km depth are shown. (a) temperature, (b) pressure, (c) density, (d) thermal conductivity, (e) viscosity, (f) strain rate. The position of the profiles is shown in Figure 3 (c).

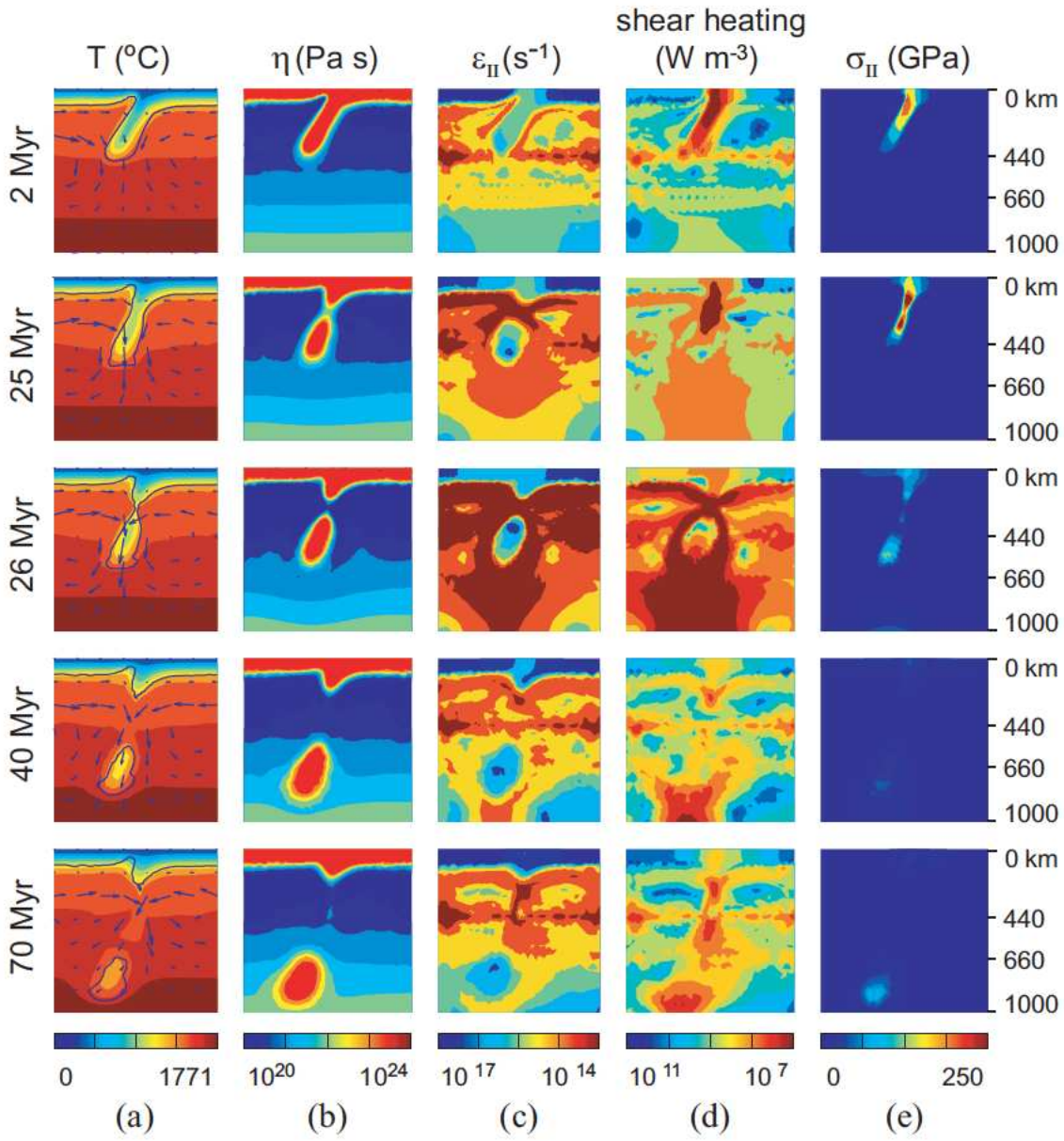


**Fig. 5** Evolution of the detachment calculated with the reference model. (a) Temperature, velocity and level set position, (b) viscosity, (c) strain rate second invariant, (d) shear heating, (e) stress second invariant.

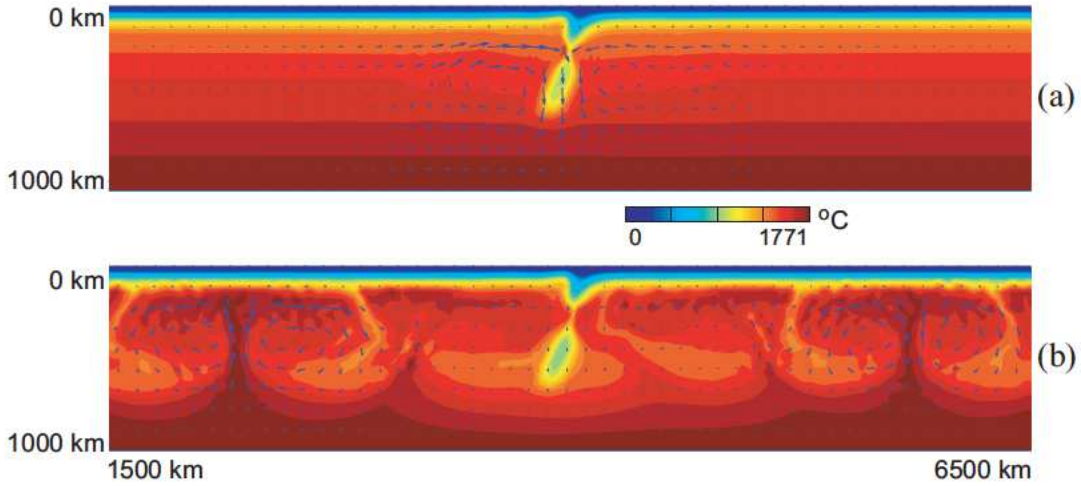


**Fig. 6** Comparison of the thermal state of the model with (a) and without (b) accounting for the adiabatic heating term in the energy balance equation.

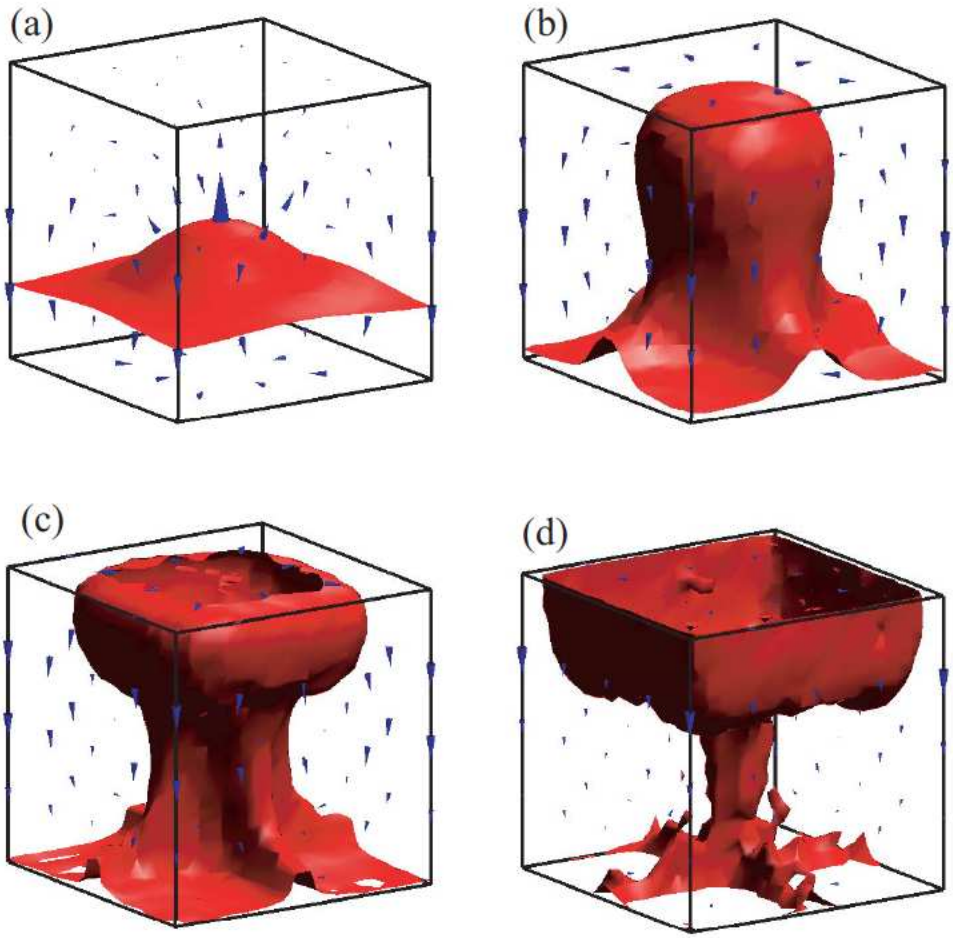


**Fig. 7** Evolution of a Rayleigh–Taylor instability. The red surface is the interface between two materials described by the level set. The blue triangles indicate the velocity directions and magnitude. The viscosity ratio is $\eta_1/\eta_2 = 1$ and the initial lower layer thickness $h = 1/3$

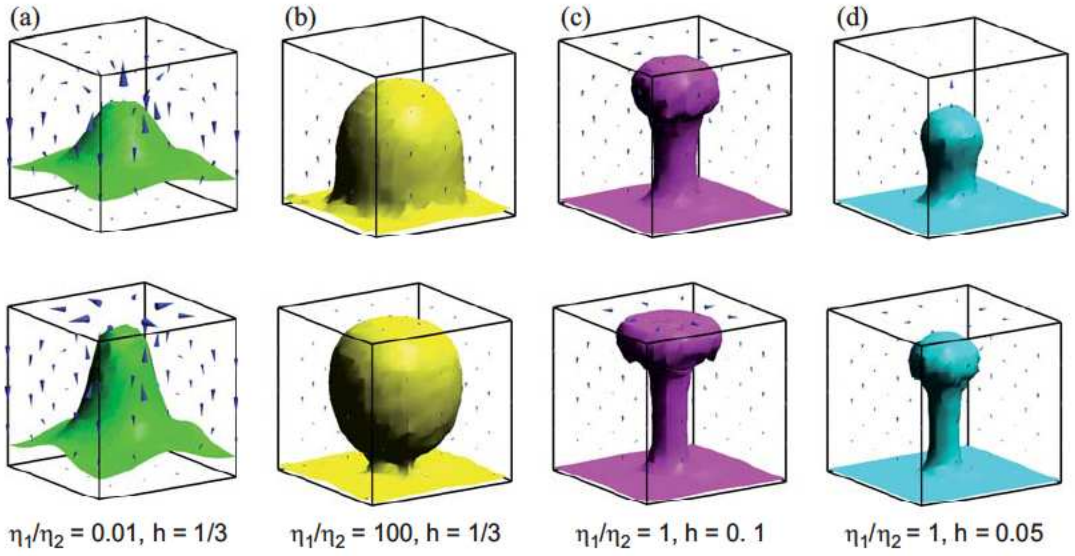


**Fig. 8** Two snapshots of the evolution of four different Rayleigh–Taylor instabilities. The viscosity ratios and thickness $h$ of the lower layer determines the shape of the plume.

| Symbol | Meaning | Value used | Dimension |
|---|---|---|---|
| $\mathbf{g}$ | gravity acceleration vector | (0,-9.8) | m $s^{-1}$ |
| $R$ | gas constant | 8.314510 | J $K^{-1}$ $mol^{-1}$ |
| $T_0$ | reference temperature | 273 | K |
| $p_0$ | reference pressure | 0.1 | MPa |
| $\rho_{ol}$ | reference density | 3300 | kg $m^{-3}$ |
| $\alpha$ | thermal expansion coefficient | $3 \times 10^{-5}$ | $K^{-1}$ |
| $\beta$ | compressibility coefficient | $5 \times 10^{-5}$ | $MPa^{-1}$ |
| $C_p$ | thermal capacity | 1200 | J $kg^{-1}$ $K^{-1}$ |
| $f_r$ | radiogenic heat production | 0 | W $m^{-1}$ |
| $S_{es}$ | Clapeyron slope for the 410 phase change | 2.5 | MPa $K^{-1}$ |
| $S_{per}$ | Clapeyron slope for the 660 phase change | -2.5 | MPa $K^{-1}$ |
| $T_{es}$ | reference temperature of the 410 phase change | 1700 | K |
| $T_{per}$ | reference temperature of the 660 phase change | 1873 | K |
| $p_{es}$ | reference pressure of the 410 phase change | 13500 | MPa |
| $p_{per}$ | reference pressure of the 660 phase change | 23100 | MPa |
| $\Delta\rho_{es}$ | density increment at the 410 phase change | 250 | kg $m^{-3}$ |
| $\Delta\rho_{per}$ | density increment at the 660 phase change | 250 | kg $m^{-3}$ |
| | Dislocation creep | | |
| $E$ | activation energy | 540 | kJ $mol^{-1}$ |
| $V^*$ | activation volume | 14 | J $MPa^{-1}$ $mol^{-1}$ |
| $n$ | power law exponent | 3.5 | - |
| $A$ | pre–exponential factor | $7.6\times10^{-16}$ | $Pa^{-n}$ $s^{-1}$ |
| | Diffusion creep | | |
| $E$ | activation energy | 300 | kJ $mol^{-1}$ |
| $V^*$ | activation volume | 4.5 | J $MPa^{-1}$ $mol^{-1}$ |
| $n$ | power law exponent | 1 | - |
| $A$ | pre–exponential factor | $6.07\times10^{-11}$ | $Pa^{-n}$ $s^{-1}$ |

**Table 1** Notations

| | $\dot{\varepsilon}_{II}$ | | | Shear heating | | | $\sigma_{II}$ | | | Velocity | | |
|---|---|---|---|---|---|---|---|---|---|---|---|---|
| Model | max | time | depth | max | time | depth | max | time | depth | max | time | depth |
| | $s^{-1}$ | Myr | km | $Wm^{-3}$ | Myr | km | MPa | Myr | km | cm $yr^{-1}$ | Myr | km |
| *ref* | $7.6\times10^{-14}$ | 26 | 243 | $1.1\times10^{-5}$ | 26 | 252 | 423 | 23 | 158 | 10.1 | 26 | 400 |
| *noSH* | $2.4\times10^{-14}$ | 40 | 278 | 0 | - | - | 450 | 35 | 158 | 3.5 | 40 | 423 |
| *noAH* | $5.2\times10^{-14}$ | 25 | 468 | $1.1\times10^{-5}$ | 22 | 208 | 565 | 19 | 166 | 29.3 | 23 | 397 |
| *no410* | $3.2\times10^{-14}$ | 48 | 253 | $5.0\times10^{-6}$ | 47 | 224 | 230 | 38 | 147 | 4.7 | 48 | 239 |
| *no660* | $6.8\times10^{-14}$ | 26 | 219 | $2.4\times10^{-5}$ | 26 | 235 | 428 | 23 | 166 | 9.2 | 26 | 223 |
| *max* $\eta$ | $8.2\times10^{-14}$ | 41 | 220 | $1.6\times10^{-5}$ | 41 | 241 | 456 | 25 | 130 | 10.86 | 41 | 400 |
| *lith70* | $1.3\times10^{-13}$ | 23 | 184 | $3.1\times10^{-5}$ | 23 | 184 | 273 | 21 | 107 | 16.8 | 23 | 383 |

**Table 2** Maximum values for second invariant of the strain rate, shear heating, second invariant of the stress and velocity for each model. Second and third columns of each box are the time and depth where the max values are obtained. Model labels: *ref* for the reference model, *noSH* for the model without shear heating, *noAH* for the model without adiabatic heating, *no410* for the model without the 410 km depth mineral phase transition, *no660* for the model without 660 km depth mineral phase transition, *max* $\eta$ for the model with increased maximum allowed viscosity and *lith70* for the model with 70 km thick lithosphere.